ADVANCED FUNCTIONAL MATERIALS
www.afm-journal.de

Materials Views
www.MaterialsViews.com

Improving the Extraction of Photogenerated Electrons with SnO_2 Nanocolloids for Efficient Planar Perovskite Solar Cells

Hua-Shang Rao, Bai-Xue Chen, Wen-Guang Li, Yang-Fan Xu, Hong-Yan Chen, Dai-Bin Kuang, and Cheng-Yong Su*

Great attention to cost-effective high-efficiency solar power conversion of trihalide perovskite solar cells (PSCs) has been hovering at high levels in the recent 5 years. Among PSC devices, admittedly, TiO_2 is the most widely used electron transport layer (ETL); however, its low mobility which is even less than that of $CH_3NH_3PbI_3$ makes it not an ideal material. In principle, SnO_2 with higher electron mobility can be regarded as a positive alternative. Herein, a SnO_2 nanocolloid sol with ≈3 nm in size synthesized at 60 °C was spin-coated onto the fuorine-doped tin oxide (FTO) glass as the ETL of planar $CH_3NH_3PbI_3$ perovskite solar cells. $TiCl_4$ treatment of SnO_2-coated FTO is found to improve crystallization and increase the surface coverage of perovskites, which plays a pivotal role in improving the power conversion efficiency (PCE). In this report, a champion efficiency of 14.69% (J_{sc} = 21.19 mA cm^{-2}, V_{oc} = 1023 mV, and FF = 0.678) is obtained with a metal mask at one sun illumination (AM 1.5G, 100 mW cm^{-2}). Compared to the typical TiO_2, the SnO_2 ETL efficiently facilitates the separation and transportation of photogenerated electrons/holes from the perovskite absorber, which results in a significant enhancement of photocurrent and PCE.

1. Introduction

Recently, the research of the organometal trihalide perovskite solar cells have advanced by leaps and bounds, especially in the field of pursuing cost-effective high-efficiency solar power conversion.[1] Relying on pivotal advantages of wide absorption range,[2] high extinction coefficient,[3] and long electron-hole diffusion length,[4] the organometal trihalide perovskites have been regarded as the most promising materials for solar energy conversion.[3a,5] To date, the power conversion efficiency (PCE) of perovskite solar cells (PSCs) has skyrocketed from pristine ≈10% with solid-state organic hole transport materials [1,3b] to the highest of 20.1%,[6] which showed incredible momentum of development and potential value of application. The typical PSC structures are composed of five functional layers as shown in **Scheme 1**. Upon light illumination, both free carriers (electrons and holes) and weakly bound excitons should been generated in $CH_3NH_3PbI_3$ with interchange being possible between the two populations at ambient temperature because of the low exciton binding energy.[7] The free electrons are injected to conduction band (CB) of electron transport materials (ETM) such as TiO_2 or ZnO within ps or fs, and then transport to conducting oxide electrode (fluorine-doped tin oxide (FTO) or indium tin oxide (ITO)), while the free holes transfer simultaneously to hole transport materials (HTM, such as spiro-OMeTAD, PTAA,[8] CuI,[9] CuSCN,[10] etc.) and cathode (Au, Ag, and C[11]) successively. The perovskites are well known to behave ambipolar characteristics,[12] implying that the HTM layer is unnecessary sometimes.[13] Aforementioned charge injection and transformation process were previously investigated by transient fluorescence spectroscopy and photoconductance measurements.[14] Typically, there are seven recombination pathways (**a–g**) in PSC, among which the electron quenching (**a**), trapping (**b**,**c**), and recombining with the perovskite (**d**) and HTM (**e**) strongly rely on the quality of ETM and perovskites, while the other process **g** and **f** relate directly to the coverage of ETM on the TCO surface and perovskite on the ETM, respectively. Hence, it is essential to accelerate the electron transport in ETM and decrease the above recombination processes for improving the photovoltaic performance of PSCs.

Although TiO_2 is the most widely used electron transport layer (ETL) material for PSCs,[15] the low mobility (0.1–1 cm^2 V^{-1} s^{-1}[16] which is even less than $CH_3NH_3PbI_3$ (20–30 cm^2 V^{-1} s^{-1}[17] makes it not an ideal material. Therefore, searching for electron transport material which has higher electron mobility and conductivity is substantial to improve the electron transfer process of PSC, such as the usage of ZnO,[18] AZO,[19] Y-TiO_2,[20] and Nb-TiO_2.[21] Compositing with graphene[22] is another method to improving performance by providing superfast electron tunnel and reducing series resistance. SnO_2,[23] whose electron mobility is about 100–200 cm^2 V^{-1} s^{-1},[24] higher one and two magnitude than $CH_3NH_3PbI_3$ and TiO_2, must be one of the promising ETL

H.-S. Rao, B.-X. Chen, W.-G. Li, Y.-F. Xu,
Dr. H.-Y. Chen, Prof. D.-B. Kuang, Prof. C.-Y. Su
MOE Key Laboratory of Bioinorganic
and Synthetic Chemistry
State Key Laboratory of Optoelectronic
Materials and Technologies
Lehn Institute of Functional Materials
School of Chemistry and Chemical Engineering
Sun Yat-sen University
Guangzhou 510275, P. R. China
E-mail: kuangdb@mail.sysu.edu.cn

DOI: 10.1002/adfm.201501264

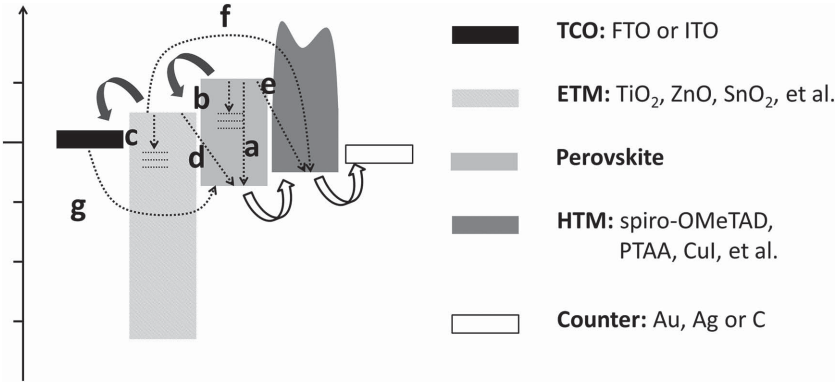

Scheme 1. A schematic diagram of device structure for mesoporous and planar PSCs (except perovskite/PCBM structure). The compact and/or mesoporous electron transport materials are considered as the electron transport layer (ETL). The electron and hole transfer processes are indicated by arrows.

materials for PSC. Herein, the SnO_2 nanocolloid (3 nm in size) solution prepared through precursors reflux was spin-coated onto the clean FTO glass as ETL for $CH_3NH_3PbI_3$ planar PSC demonstrating the champion efficiency of 14.69% (J_{sc} = 21.19 mA cm^{-2}, V_{oc} = 1023 mV, and FF = 0.678) is obtained which measured with a metal mask (area: 0.1256 cm^2) under one sun illumination (AM 1.5G 100 mW cm^{-2}). Furthermore, the photovoltaic performance of PSC based on SnO_2 ETL (14.69%) is significantly superior to that of TiO_2 (PCE: 13.37%).

2. Results and Discussion

The compact SnO_2 ETL was implemented by spin-coating the as-synthesized SnO_2 colloidal solution composed of less than 3 nm nanoparticles (Figure S1, Supporting Information) on a clean FTO conducting glass and sintered at 500 °C for 1 h to remove organics and improve crystallinity. The resulting SnO_2 compact layer was used directly as ETL or followed with $TiCl_4$ treatment of different times before the perovskite deposition. The $CH_3NH_3PbI_3$ absorber was deposited by one-step spin-coating of a $PbCl_2$ and CH_3NH_3I mixture dissolved in dimethylformamide (DMF) and annealing at 95 °C for 2 h. The monolithic cell fabrication is completed by spin coating typical organic HTM named spiro-MeOTAD and then sputtering an Au cathode.

2.1. Structure of Device

The SnO_2-based planar PSC device had a sandwich-like configuration with the SnO_2 layer, perovskite layer, HTM layer, and Au as thick as 100, 200, 150, and 100 nm, respectively. The typical cross-sectional SEM image of the planar PSC (**Figure 1**a) and its energy dispersive spectroscopy mapping of Pb, I, and C clearly shows the vertical distribution of Pb and I corresponds to perovskite. XRD patterns (Figure 1b) conform to the mixture of the perovskites depositing on SnO_2 compact layer. Four characteristic peaks could be identified (27°, 34°, 38°, and 52°) and are assigned to the (110), (101), (200), and (211) facet of SnO_2 (JCPDS Card No. 71-0652), shown as black curve. The other characteristic peaks estimated at 14.2°, 28.5°, 31.8°, 43.2°, and 58.8° (red curve) are indexed to the (110), (220), (310), (330), and (440) planes of the $CH_3NH_3PbI_3$ phase.[4,25] Although chlorine anion has been provided by $PbCl_2$ in precursor, which can be released by gaseous CH_3NH_3Cl (or other organic chlorides),[26] instead of occupying the lattice of $CH_3NH_3PbI_3$ phase,[27] the EDS result (Figure S2, Supporting Information) shows there is no chlorine signal in the perovskite film. Hence, the chlorine anion of perovskite precursor merely influences the growth of the $CH_3NH_3PbI_3$[27,28] and improves diffusion length of electron and hole (or the weakly bound exciton).[7a,29]

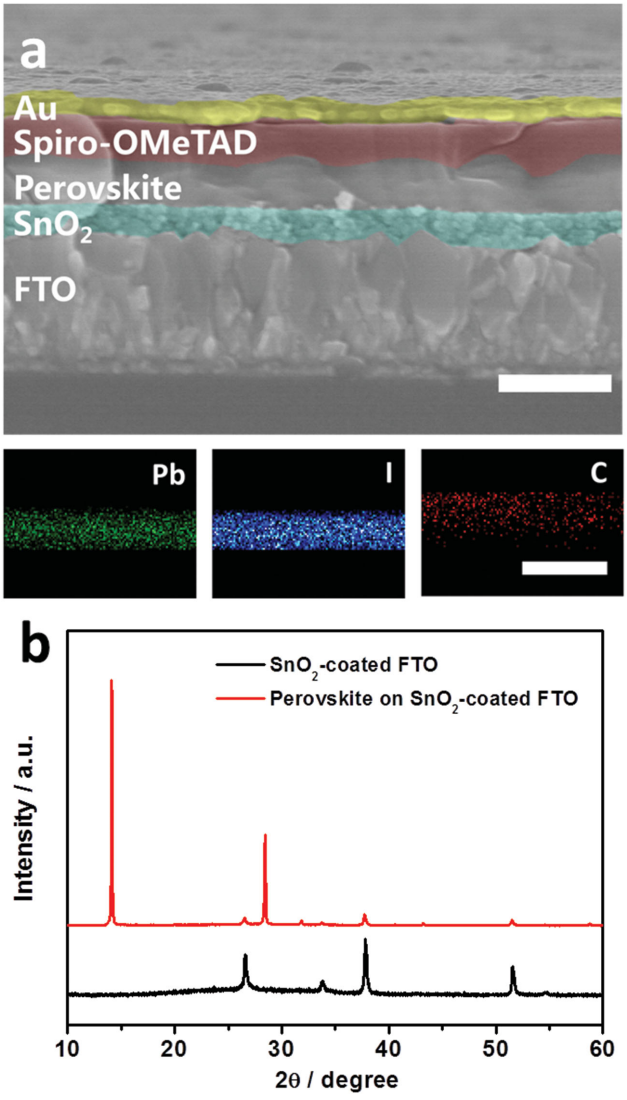

Figure 1. a) The color-enhanced cross-sectional SEM micrograph and energy dispersive spectroscopy (EDS) mapping of typical PSC based on SnO_2-coated FTO. Here the scale bar corresponds to 500 nm. b) XRD patterns of SnO_2-coated FTO (black) and coating with perovskite (red).

Table 1. The average values of photovoltaic parameters and maximum PCE for 30 devices, which are extracted from measuring current density–voltage curves at simulated one sun illumination (100 mW cm^{-2}, AM 1.5G).

Cell	J_{sc} [mA cm^{-2}]	V_{oc} [mV]	FF	PCE [%]	Maximum PCE [%]
SnO_2	18.8	647	0.418	5.12	6.52
SnO_2–$TiCl_4$(1)	19.5	963	0.589	11.06	12.73
SnO_2–$TiCl_4$(2)	20.0	997	0.670	13.38	14.69
SnO_2–$TiCl_4$(3)	19.7	974	0.606	11.60	12.35

2.2. Photovoltaic Performance of PSCs

The current density–voltage (J–V) characteristics of the PSCs with different times of $TiCl_4$ treatment (0–3) were investigated in dark and under simulated one sun illumination (AM 1.5G). The active area of the all solar cells was determined by a metal mask (0.1256 cm^2). The average values of the photovoltaic performance parameters are further displayed in **Table 1** and their statistical distribution shown in Figure S3 (Supporting Information). J–V curves of the typical SnO_2 ETL based planar PSCs are shown in **Figure 2**a. It is noteworthy that the average PCEs of SnO_2 ETL treated with $TiCl_4$ for once (SnO_2–$TiCl_4$(1)) or twice (SnO_2–$TiCl_4$(2)) are 11.06% and 13.38%, respectively, which are significantly higher than that of without $TiCl_4$ treated SnO_2 (5.12%). The enhancement came mainly from the improvement in the short-circuit density (J_{sc}) from 18.8 to 20.0 mA cm^{-2}, open circuit voltage (V_{oc}) from 647 mV to 997 mV and fill factor (FF) from 0.418 to 0.670, respectively. The incident photon-to-electron conversion efficiency (IPCE) or external quantum efficiency of these SnO_2-based devices are presented in Figure 2b, which reveal that IPCE values of $TiCl_4$ treatment based devices are higher than that of SnO_2 cell in the whole wavelength from 400 to 780 nm. The maximum values from IPCE spectra are 81.8%, 84.4%, 86.2%, and 85.6% for the four typical devices, whose change is excellent agreement with the measured J_{sc}. The obvious generation of photocurrent starts at 780 nm coincides to the bandgap of the $CH_3NH_3PbI_3$.

To elucidate the effects of $TiCl_4$ treatment on the photovoltaic performance, the surface morphology of perovskite, series resistances (R_s), and shunt resistances (R_{sh}) are further discussed as follows. **Figure 3**a is the SEM image of the SnO_2 sample without $TiCl_4$ treatment showing pinholes and infertile perovskite coverage and pinholes that result in less perovskite coverage. However, after the $TiCl_4$ treatment for twice (SnO_2–$TiCl_4$ (2)), the perovskite particles form smooth and uniform film where only bits of pinholes formed and the coverage ratio of perovskite raised (Figure 3c). The reason why $TiCl_4$ treatment could aggrandize the perovskites' coverage was investigated through a contact angle measurement by dropping a drop of DMF on FTO–SnO_2 and FTO–SnO_2–$TiCl_4$(2). Figure 3b,d shows the photographs of DMF contact angle for FTO–SnO_2 and FTO–SnO_2–$TiCl_4$(2) samples indicating the enhancement of wettability induced by $TiCl_4$ treatment resulting in the smaller contact angle for the latter which helps to form smooth, conformal perovskites films and hence improve the surface coverage. To exclude the effect of $TiCl_4$ treatment toward the phase purity of perovskites, XRD characterization was performed which proved that the $TiCl_4$ treatment only influenced the surface coverage owing to the uniform XRD patterns shown in Figure S4 (Supporting Information).

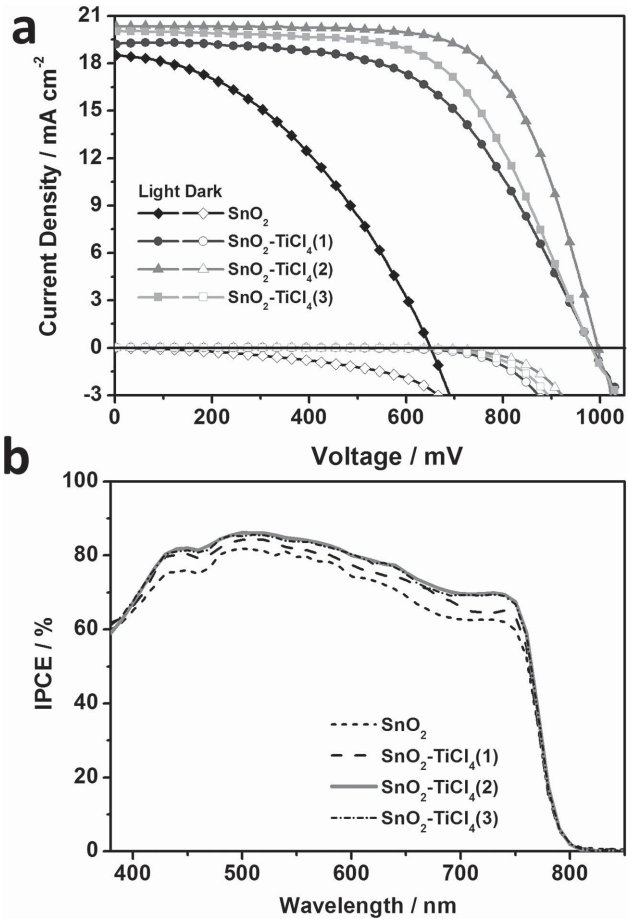

Figure 2. a) The J–V curves of typical planar perovskite solar cells based on a SnO_2-based ETM layer with or without $TiCl_4$ treatment measured under illumination (solid) or in dark (hollow). b) Incident photon-to-current conversion efficiency (IPCE) of typical perovskite solar cells.

Imperfect surface coverage of perovskite on SnO_2-coated FTO leads to the direct contact of HTM and ETM which results in the current leakage as shown in Scheme 1, process **f**. Large particle and uniform film reduce the quenching and trapping at surface of perovskite (process **a** and **b**). In addition, $TiCl_4$ treatment can decrease surface defect of SnO_2 which was verified to improve the performance of DSSC[30] due to the decreased recombination process **c**. Similarly, coating SnO_2 with TiO_2 layer which has more positive conduction band can impede recombination between conduction band of SnO_2 and valance band of $CH_3NH_3PbI_3$ (process **d**). Such a staggered energy band alignment and thin thickness hamper imperceptibly the injection and transport of photogenerated electrons. The J–V curves measured in dark show the onset of the dark current for SnO_2 cell is from very low bias (≈300 mV), while the others with $TiCl_4$ treatment shift to ≈700 mV bias (Figure 2a). Such dramatic shift of bias implies a decline in the recombination between $CH_3NH_3PbI_3$, HMT, and ETL (process **d** and **f**) as well

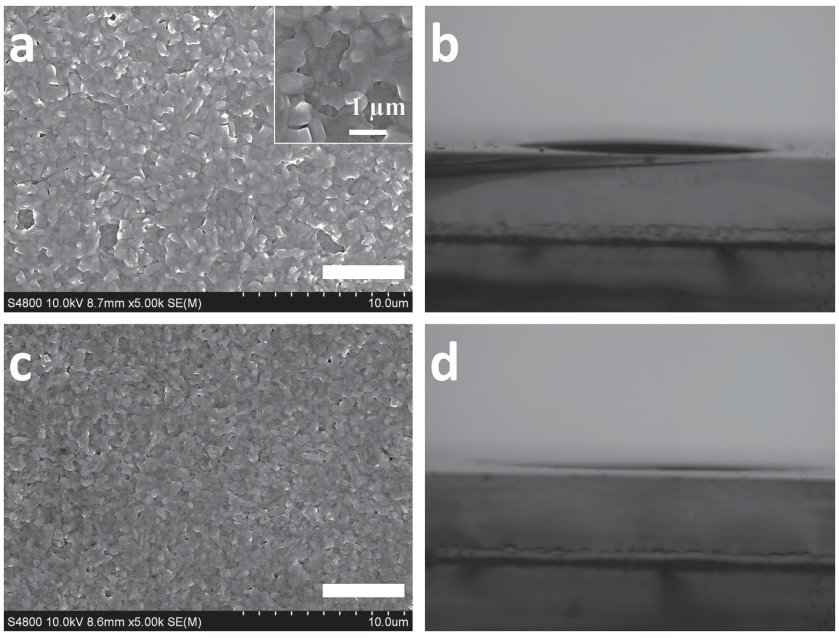

Figure 3. Top-view SEM images of perovskite films coated on a) FTO–SnO_2 and c) FTO–SnO_2–$TiCl_4$(2). Here the scale bar corresponds to 5 μm. b) DMF contact angles of SnO_2 and d) SnO_2–$TiCl_4$(2) samples by putting a drop of DMF on the substrates with syringe needle of 0.26 mm.

as by surface traps (process **c**) for the $TiCl_4$ treated SnO_2 samples. Hence, the significant improvement of 350 mV (about increase of 54%) in V_{oc} for SnO_2–$TiCl_4$(2) solar cell compared to that of SnO_2 is ascribed to the amelioration of recombination in processes **c**, **d**, and **f**, which are responsible for the significant enhancement of the power conversion efficiency (from 5.12% to 13.38%, Table 1). Very exciting, the champion power conversion efficiency of PSC based on SnO_2–$TiCl_4$(2) ETL is 14.69% accompanying with J_{sc}, V_{oc}, and FF being 21.29 mA cm^{-2}, 1023 mV, and 0.678, respectively (Figure S5, Supporting Information).

Both forward and reverse bias sweep were used to evaluate the hysteresis behavior of PSCs.[31] Figure S6 (Supporting Information) shows the *J–V* curves of perovskite solar cells based on SnO_2–$TiCl_4$(2) which were performed from forward bias to short circuit (FB-SC) and from short circuit to forward bias (SC–FB) with different scan rates from 1.00 to 0.15 V s^{-1}. The detailed performance parameters obtained from these *J–V* curves are further displayed in Table S1 in the Supporting Information. For the SC–FB measurement, the PCEs decreases from 14.19% to 11.25% (with scan rate variation from 1.00 to 0.15 V s^{-1}) showing strong scan rate dependence. The key factor is the decrease of FF (from 0.693 to 0.565). However, the PCEs of FB-SC possess small range of oscillation (from 14.66% to 14.38%). Such results reveal the unapparent hysteresis of *J–V* curves for the both SC–FB and FB–SC under fast scan rate condition which is similar to the previous planar PSCs.[31b,32] As hysteresis behavior possibly comes from unbalanced charge transportation and collection,[33] perovskite's ferroelectricity,[34] ion migration, or defects,[31b] the steady-state power output at a given constant forward bias is another important parameter to evaluate the power conversion efficiency. As shown in **Figure 4**a, the device exhibits FB–SC performance with J_{sc} = 20.54 mA cm^{-2}, V_{oc} = 1027 mV, FF = 0.683 and PCE = 14.38%, and SC–FB performance with J_{sc} = 20.48 mA cm^{-2}, V_{oc} = 973 mV, FF = 0.565 and PCE = 11.25% at a scan rates of 0.15 V s^{-1}. Figure 4b shows the steady-state current measured at forward bias 800 mV and stabilized power output under simulated AM 1.5G sunlight of 100 mW cm^{-2}. The PCE rises to the maximum value with 13.53% at 80 s and then shows a negligible decrease after 500 s illumination which is 94% of the PCE at FB–SC scan direction. For comparison, the stabilized power output at forward bias 450 mV of the PSC based on SnO_2 (without $TiCl_4$ treatment) is 5.20%, which is 92% of the PCE at FB–SC scan direction (Figure S7, Supporting Information).

To elucidate the FF variation of the various PSCs, the series resistance (R_s) and the shunt resistance (R_{sh}) are extracted from the *J–V* curves. **Figure 5**a,b presents the R_s and R_{sh} of SnO_2 nanocolloid based PSCs with different treatment times (0–3) of $TiCl_4$. It is conspicuous that the additional $TiCl_4$ treatment results in the decrease of R_s from 12.9, 10.8 to 9.8 Ω cm^2 for the SnO_2, SnO_2–$TiCl_4$ (1), and SnO_2–$TiCl_4$(2) cell, respectively. On the contrary, the R_{sh} increases by one order of magnitude for the SnO_2–$TiCl_4$(2) cell compared with the sole SnO_2 film thanks to the reduced recombination resulting from the increasing perovskite coverage. However, there is a sharp increase of R_s for the SnO_2–$TiCl_4$(3) cell, which was 50% more than that of the SnO_2–$TiCl_4$(2) cell, meanwhile the R_{sh} of SnO_2–$TiCl_4$(2) and SnO_2–$TiCl_4$(3) cells are in the same order of magnitude. Such result is ascribed to the thicken TiO_2 coating via $TiCl_4$ treatment above twice (Figure S8, Supporting Information). Consequently, there was no doubt that average fill factor (FF) increased obviously about 60% from 0.418 (sole SnO_2) to 0.670 (SnO_2–$TiCl_4$(2)) but decreased to 0.606 for SnO_2–$TiCl_4$(3) cell.

Generally, the amelioration of surface coverage of perovskite will improve the absorbance of devices. The onset absorption of perovskite deposited on the four samples starts at ≈780 nm (Figure S9a, Supporting Information) which conforms to the IPCE (Figure 1b), and the absorbance is enhanced through $TiCl_4$ treatment. This variation tendency accords with the tendency of J_{sc} mainly. However, the light absorption efficiency of the four cells may not have significant difference because of high extinction coefficient of perovskite hence the transmission is less than 30% for all samples range from ≈780 nm (Figure S9b, Supporting Information). Furthermore, the light absorption can be enhanced by reflection of sputtered Au layer which further decreases the discrepancy in light absorption of the four samples. In a word, the small variation of absorbance affects J_{sc} weakly. It is noteworthy that the almost three time enhancement of power conversion efficiency for the SnO_2–$TiCl_4$(2) cell (13.38%) compared to the SnO_2 cell (5.12%) is mainly ascribed to the significant augments of V_{oc} (54%) and FF (60%) and a slight rise of J_{sc} (6%).

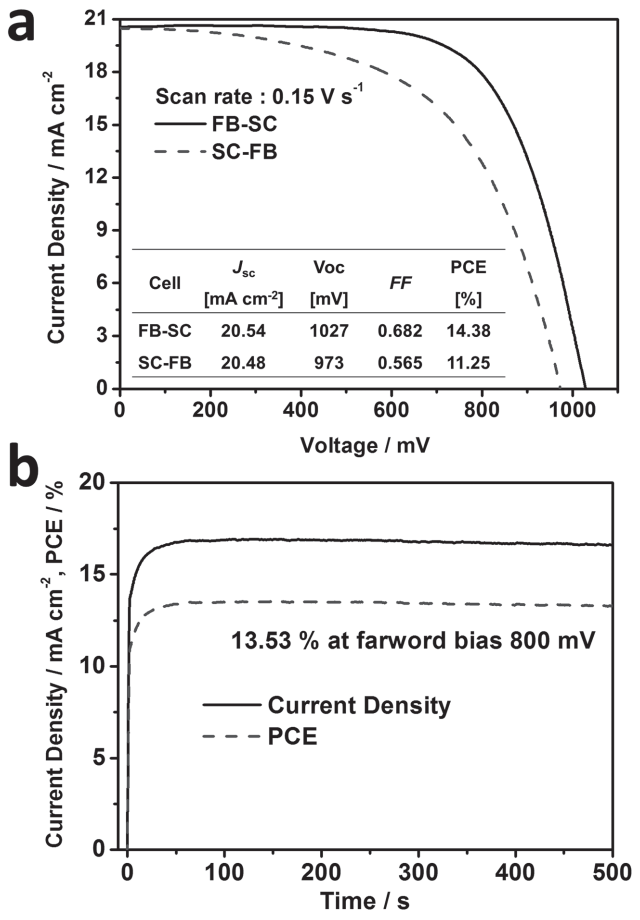

Cell	J_{sc} [mA cm^{-2}]	Voc [mV]	*FF*	PCE [%]
FB-SC	20.54	1027	0.682	14.38
SC-FB	20.48	973	0.565	11.25

Figure 4. a) The *J–V* curves and photovoltaic parameters were performed from forward bias to short circuit (FB–SC) and from short circuit to forward bias (SC–FB) at a scan rate of 0.15 V s^{-1} for the PSC based on SnO_2–$TiCl_4$(2). b) Steady-state current measured at forward bias 800 mV and stabilized power output under simulated AM 1.5G sunlight of 100 mW cm^{-2}.

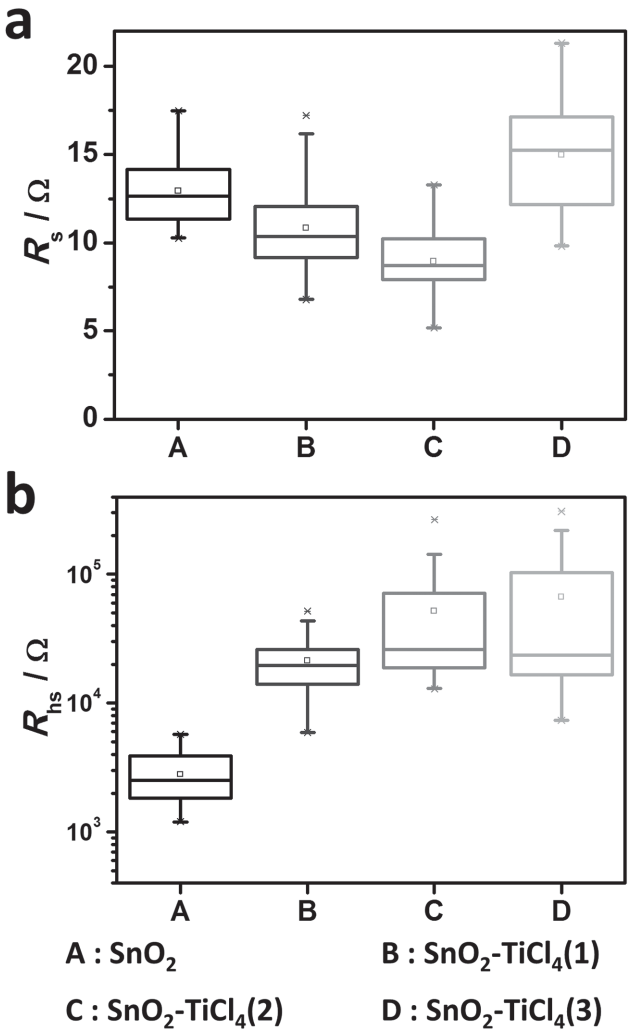

Figure 5. a) Series resistances (R_s) and b) Shunt resistances (R_{hs}) of the PSCs based on various SnO_2 electron collection layer.

2.3. Comparison of SnO_2 and TiO_2

As shown in **Figure 6**a, as the CB of SnO_2 is about 0.5 eV more negative than that of TiO_2,[35] thus suggests that the photogenerated electrons injection from the $CH_3NH_3PbI_3$ to SnO_2 could be faster than the TiO_2 counterpart. In addition, the significant higher electron mobility of SnO_2 would help to extract and transport photogenerated electrons from the $CH_3NH_3PbI_3$ absorber efficiently to collecting electrode. To study the process of electron-hole's actions, the samples of the independent perovskite film, SnO_2/Perovskite, SnO_2–$TiCl_4$(2)/Perovskite, and TiO_2–$TiCl_4$(2)/Perovskite were prepared on blank glass for photoluminescence (PL). The PL measurements were performed to evaluate whether SnO_2 film efficiently extract photogenerated electron from the perovskite absorber. Figure 6b shows the steady-state PL spectra of SnO_2/perovskite, SnO_2–$TiCl_4$(2)/perovskite, TiO_2–$TiCl_4$(2)/perovskite as well as the independent perovskite deposited on blank glass. Obviously, the $CH_3NH_3PbI_3$ perovskite film shows a considerably greater degree of PL quenching when on SnO_2–$TiCl_4$(2) as compared to TiO_2–$TiCl_4$(2), proving SnO_2 enhanced electron injection, collection, and transport efficiency, which follows naturally from the negative conduction band and increased electron mobility. At the same time, SnO_2/perovskite shows slight greater degree of PL quenching than SnO_2–$TiCl_4$(2)/perovskite. Furthermore, Figure 6c further presents the time-resolved photoluminescence (TRPL) curves of these samples, of which the fitted time constants τ_e (associate with the electron-hole lifetime of perovskite) are 39.81, 2.87, 1.73, and 1.34 ns, respectively. The steady-state PL and TRPL results elucidated that the SnO_2 layer is more likely to accelerate light-induced charge separation, which is highly consistent with the energy levels and electron mobility of SnO_2 in contrary to TiO_2. Although a thin TiO_2 layer coated on SnO_2 perhaps mildly affect charge action, SnO_2–$TiCl_4$(2) still shows excellent ability as well as SnO_2 to extract and transport photogenerated electrons from the perovskite absorber efficiently.

To elucidate the effect of TiO_2 and SnO_2 electron extracting and transporting layer on the PSC photovoltaic performance, the two cells based on SnO_2–$TiCl_4$(2) and TiO_2–$TiCl_4$(2) ETL are investigated. The average J_{sc} of SnO_2–$TiCl_4$(2) cell

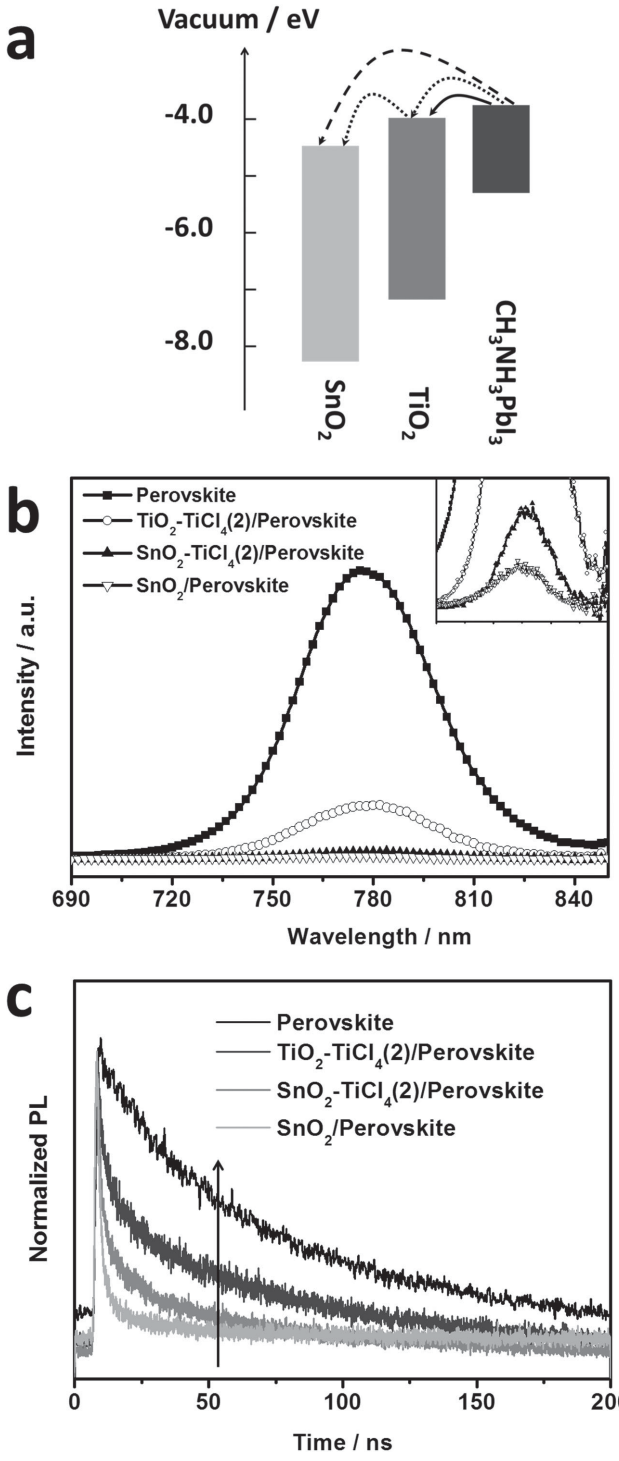

Figure 6. a) Schematic diagram illustrating the energy levels of the conduction band (CB) and valence band (VB) of TiO_2, SnO_2, and perovskite ($CH_3NH_3PbI_3$). The solid (TiO_2–$TiCl_4$(2)/perovskite), dot (SnO_2–$TiCl_4$(2)/perovskite), and dash (SnO_2/perovskite) arrows scheme electron injection and transport process of electron. b) Photoluminescence (PL) spectra (excitation at 406.2 nm) (inset is the magnified spectra) and c) time-resolved photoluminescence (TRPL) (excitation at 406.2 nm and emission at 760 nm) of the bare perovskite film and on top of TiO_2–$TiCl_4$(2), SnO_2–$TiCl_4$(2) and SnO_2.

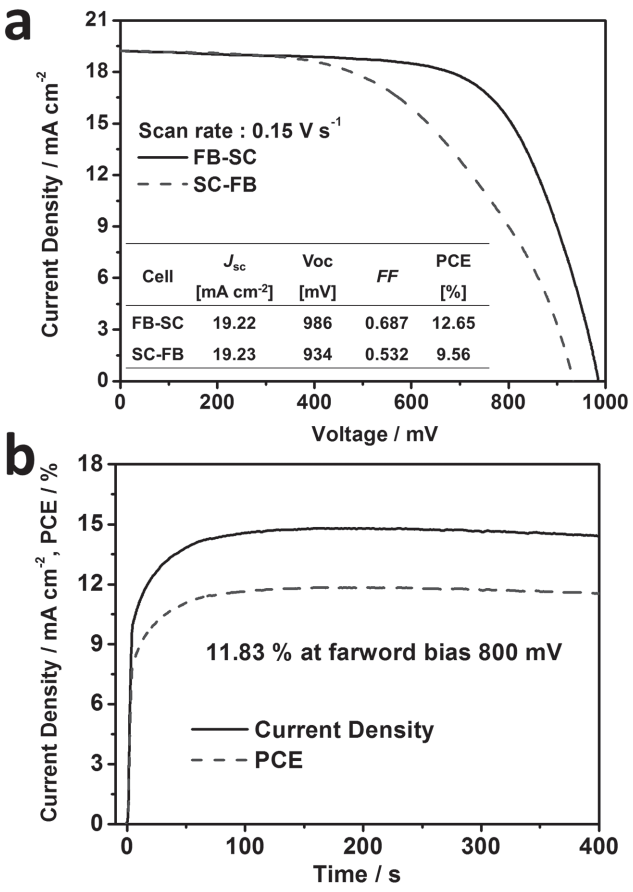

Figure 7. a) The *J–V* curves and photovoltaic parameters were performed from forward bias to short circuit (FB–SC) and from short circuit to forward bias (SC–FB) at a scan rates of 0.15 V s^{-1} for the PSC based on TiO_2–$TiCl_4$(2). b) Steady-state current measured at forward bias 800 mV and stabilized power output under simulated AM 1.5G sunlight of 100 mW cm^{-2}.

(20.0 mA cm^{-2}) is much higher than that of TiO_2–$TiCl_4$(2) counterpart (18.9 mA cm^{-2}; Table S2 and Figure S10, Supporting Information). The increase (1.1 mA cm^{-2}) in J_{sc} must be ascribed to the enhanced injection process of the photogenerated electrons from perovskite to CB of electron transport materials (ETM) and fast electron transportation process. The SnO_2–$TiCl_4$(2) cell shows an enhancement of PCE (13.37%) than that of the TiO_2 counterpart (12.33%) with weakly enhanced V_{oc} and FF. Meanwhile, the two cells based on SnO_2–$TiCl_4$(2) and TiO_2–$TiCl_4$(2) ETL show same scan rate dependence (Figure S11 and Table S3, Supporting Information). As shown in **Figure 7**a, the TiO_2–$TiCl_4$(2) cell exhibits FB-SC performance with J_{sc} = 19.22 mA cm^{-2}, V_{oc} = 986 mV, FF = 0.687 and PCE = 12.65%, and SC-FB performance with J_{sc} = 19.23 mA cm^{-2}, V_{oc} = 934 mV, FF = 0.532 and PCE = 9.56% at a scan rates of 0.15 V s^{-1}. In contrast with the SnO_2–$TiCl_4$(2) cell, it shows similar hysteresis behavior. In the same time, the stabilized power output at forward bias 800 mV of the TiO_2–$TiCl_4$(2) cell is 11.83% (Figure 7b) which is 94% of the PCE at FB-SC scan direction. Both J_{sc} of FB-SC and SC–FB scan direction and stabilized power output of the SnO_2–$TiCl_4$(2) cell are

higher than the values of the TiO_2–$TiCl_4$(2) counterpart. Hence, the enhancement of the photocurrent and photovoltaic performance for SnO_2–$TiCl_4$(2) cell benefits from the improvement of extraction of photogenerated electrons by SnO_2.

3. Conclusion

In summary, reproducible and high-efficiency $CH_3NH_3PbI_3$ perovskite solar cells based on compact SnO_2 nanocolloid electron transportation layer are reported for the first time. The $TiCl_4$ treatment is found to form smooth and uniform film, promote the perovskite surface coverage, and reduce the recombination which directly contribute to the photovoltaic performance of the planar PSCs. Consequently, a champion efficiency of 14.69% (J_{sc} = 21.19 mA cm^{-2}, V_{oc} = 1023 mV, and FF = 0.678) is achieved for the twice $TiCl_4$ treated SnO_2 ETL which measured with a metal mask under one sun illumination (AM 1.5G 100 mW cm^{-2}). Compared to the typical TiO_2, the present SnO_2 ETL facilitates the separation and transportation of photogenerated electrons/holes from the perovskite absorber efficiently due to the negative conduction band and high electron mobility, which results in significant enhancement of the photovoltaic performance than that of TiO_2 ETL (champion efficiency of 13.37%). The current study not only reveals that the SnO_2 can be an appropriate electron extraction and transportation material for the efficient perovskite solar cells, but also points out that the other materials with high electron mobility, conductivity, and appropriate energy band will have great potential to boost the power conversion efficiency in mesoporous or planar perovskite solar cells.

4. Experimental Section

Materials Synthesis: SnO_2 colloidal solution was prepared via precursors reflux. 11.39 mL $SnCl_4$ (Aldrich) was dropped in mixed solution consists of 3.41 mL acetylacetone and 12.54 mL *n*-butanol and kept stirring for 15 min. Then 1.27 g *para*-toluene-sulfonic acid (dissolved in 6 mL deionized water) was added to the solution and refluxed at 60 °C for 12 h. CH_3NH_3I was synthesized by blending methylamine (33 wt% in methanol) and hydroiodic acid (57 wt% aqueous) with a molar ratio of 1.5:1 in ice-water bath for 2 h, then crystallized by spin steaming and purify by recrystallization with diethyl ether. It was dried in vacuum and stored in N_2 atmosphere.

Cells Fabrication: Briefly, FTO glass (8 Ω sq^{-1}) was prepatterned with 4 M HCl and zinc powder and cleaned with deionized water, alcohol, and acetone successively via ultrasonic process. A compact SnO_2 electron transportation layer was formed by spin-coating of SnO_2 nanocolloidal solution (dilute with ethanol, v/v 1:3) at 2000 rpm for 60 s and annealing at 500 °C for 1 h in ambient air. The same spin-coating and annealing process was for TiO_2 electron transportation layer with the mere difference by replacing the SnO_2 nanocolloidal solution with titanium diisopropoxide bis(acetylacetonate) (dilute with ethanol, v/v 1:9). The $TiCl_4$ treatment was performed by soaking the SnO_2 or TiO_2-coated FTO glass into 0.04 M $TiCl_4$ aqueous solution for 30 min at 70 °C, and then sinter at 520 °C for 30 min before perovskite deposition. This $TiCl_4$ treatment process was repeated if needed. The perovskite layer was deposited by spin-coating of perovskite precursor solution (0.245 g $PbCl_2$ and 0.415 g CH_3NH_3I dissolved in 1 mL dimethylformamide (DMF)) at 5000 rpm for 60 s and then followed annealing at 95 °C for 2 h. Then a hole-transport material solution consisting of 73.2 mg 2,2′,7,7′-tetrakis-(*N*,*N*-di-*p*-methoxyphenyl-amine)-9,9′-spirobifluorene (spiro-MeOTAD), 28.8 µL 4-*tert*-butylpyridine (*t*-BP), 17.5 µL bis(trifluoromethane) sulfonimide lithium salt (Li-TFSi) solution (520 mg in acetonitrile) and 1 mL chlorobenzene was spin-coated onto the surface of perovskite at 5000 rpm for 60 s. Finally, an ≈100 nm Au layer was deposited by magnetron sputtering.

Characterization: The photovoltaic performance of PSCs were recorded using a Keithley 2400 source meter with scan rate of 0.075 V s^{-1} under one sun AM 1.5G (100 mW cm^{-2}) illumination with a solar light simulator (Oriel, Model: 91192) which calibrated with a NREL standard Si solar cell. And the active areas of all solar cells were defined by 0.1256 cm^2 metal mask. The incident photon-to-current conversion efficiency (IPCE) spectra were recorded on a Keithley 2000 multimeter as a function of wavelength from 380 to 850 nm on the basis of a Spectral Products DK240 monochromator.

The phase purity of the samples was characterized by powder X-ray diffraction (XRD) on a Bruker D8 Advance X-ray diffractometer using Cu Kα radiation (λ = 1.5418 Å). The absorption spectra were tested by UV-3600. The crystalline structure, morphologies, and elements distribution the of the samples were examined by Field emission scanning electron microscope and energy dispersive spectroscopy (FE-SEM and EDS mapping, JSM-6330F), transmission electron microscope (TEM, JEOL-2010 HR), and high-resolution transmission electron microscope (HRTEM). Contact angles were measured by contact angle system from Dataphysics (OCA20). A drop of DMF was added by syringe needle of 0.26 mm. Photoluminescence (PL) (excitation at 406.2 nm) and time-resolved photoluminescence (TRPL) (excitation at 406.2 nm and emission at 760 nm) were measured with Edinburgh Instruments LTD (FLSP920).

Supporting Information

Supporting Information is available from the Wiley Online Library or from the author.

Acknowledgements

The authors acknowledge the financial support from the National Natural Science Foundation of China (Grant No. 91433109), the Program of Guangzhou Science and Technology (Grant Nos. 2014J4100016 and 201504010031), the Fundamental Research Funds for the Central Universities, the State Key Laboratory of Optoelectronic Materials and Technologies (Sun Yat-sen University), and the NSF of Guangdong Province (Grant Nos. S2013030013474 and 2014A030313148).

Received: March 29, 2015
Revised: September 10, 2015
Published online: November 2, 2015

[1] M. M. Lee, J. Teuscher, T. Miyasaka, T. N. Murakami, H. J. Snaith, *Science* **2012**, *338*, 643.
[2] Y. Ogomi, A. Morita, S. Tsukamoto, T. Saitho, N. Fujikawa, Q. Shen, T. Toyoda, K. Yoshino, S. S. Pandey, T. Ma, S. Hayase, *J. Phys. Chem. Lett.* **2014**, *5*, 1004.
[3] a) S. Kazim, M. K. Nazeeruddin, M. Grätzel, S. Ahmad, *Angew. Chem. Int. Ed.* **2014**, *53*, 2812; b) H. S. Kim, C. R. Lee, J. H. Im, K. B. Lee, T. Moehl, A. Marchioro, S. J. Moon, R. Humphry-Baker, J. H. Yum, J. E. Moser, M. Grätzel, N. G. Park, *Sci. Rep.* **2012**, *2*, 591.
[4] Q. Dong, Y. Fang, Y. Shao, P. Mulligan, J. Qiu, L. Cao, J. Huang, *Science* **2015**, *347*, 967.
[5] H. S. Jung, N.-G. Park, *Small* **2014**, *11*, 10.

[6] a) NREL Solar Efficiency Chart, http://www.nrel.gov/ncpv/images/efficiency_chart.jpg (accessed: December 2014); b) W. S. Yang, J. H. Noh, N. J. Jeon, Y. C. Kim, S. Ryu, J. Seo, S. I. Seok, *Science* **2015**, *348*, 1234.
[7] a) S. D. Stranks, G. E. Eperon, G. Grancini, C. Menelaou, M. J. P. Alcocer, T. Leijtens, L. M. Herz, A. Petrozza, H. J. Snaith, *Science* **2013**, *342*, 341; b) M. A. Green, A. Ho-Baillie, H. J. Snaith, *Nat. Photon.* **2014**, *8*, 506; c) N.-G. Park, *Mater. Today* **2015**, *18*, 65.
[8] J. H. Noh, S. H. Im, J. H. Heo, T. N. Mandal, S. I. Seok, *Nano Lett.* **2013**, *13*, 1764.
[9] J. A. Christians, R. C. M. Fung, P. V. Kamat, *J. Am. Chem. Soc.* **2013**, *136*, 758.
[10] P. Qin, S. Tanaka, S. Ito, N. Tetreault, K. Manabe, H. Nishino, M. K. Nazeeruddin, M. Grätzel, *Nat. Commun.* **2014**, *5*, 3834.
[11] a) A. Mei, X. Li, L. Liu, Z. Ku, T. Liu, Y. Rong, M. Xu, M. Hu, J. Chen, Y. Yang, M. Grätzel, H. Han, *Science* **2014**, *345*, 295; b) Z. Li, S. A. Kulkarni, P. P. Boix, E. Shi, A. Cao, K. Fu, S. K. Batabyal, J. Zhang, Q. Xiong, L. H. Wong, N. Mathews, S. G. Mhaisalkar, *ACS Nano* **2014**, *8*, 6797.
[12] a) J. M. Ball, M. M. Lee, A. Hey, H. Snaith, *Energy Environ. Sci.* **2013**, *6*, 1739; b) J. H. Heo, S. H. Im, J. H. Noh, T. N. Mandal, C.-S. Lim, J. A. Chang, Y. H. Lee, H. j. Kim, A. Sarkar, M. K. Nazeeruddin, M. Gratzel, S. I. Seok, *Nat. Photon.* **2013**, *7*, 486.
[13] a) L. Etgar, P. Gao, Z. Xue, Q. Peng, A. K. Chandiran, B. Liu, M. K. Nazeeruddin, M. Grätzel, *J. Am. Chem. Soc.* **2012**, *134*, 17396; b) W. Abu Laban, L. Etgar, *Energy Environ. Sci.* **2013**, *6*, 3249; c) J. Shi, J. Dong, S. Lv, Y. Xu, L. Zhu, J. Xiao, X. Xu, H. Wu, D. Li, Y. Luo, Q. Meng, *Appl. Phys. Lett.* **2014**, *104*, 063901.
[14] A. Marchioro, J. Teuscher, D. Friedrich, M. Kunst, R. van de Krol, T. Moehl, M. Grätzel, J.-E. Moser, *Nat. Photon.* **2014**, *8*, 250.
[15] a) M. Liu, M. B. Johnston, H. J. Snaith, *Nature* **2013**, *501*, 395; b) J. Burschka, N. Pellet, S.-J. Moon, R. Humphry-Baker, P. Gao, M. K. Nazeeruddin, M. Gratzel, *Nature* **2013**, *499*, 316; c) J.-H. Im, I.-H. Jang, N. Pellet, M. Grätzel, N.-G. Park, *Nat. Nano* **2014**, *9*, 927.
[16] R. G. Breckenridge, W. R. Hosler, *Phys. Rev.* **1953**, *91*, 793.
[17] C. S. Ponseca, T. J. Savenije, M. Abdellah, K. Zheng, A. Yartsev, T. Pascher, T. Harlang, P. Chabera, T. Pullerits, A. Stepanov, J.-P. Wolf, V. Sundström, *J. Am. Chem. Soc.* **2014**, *136*, 5189.
[18] D. Liu, T. L. Kelly, *Nat. Photon.* **2014**, *8*, 133.
[19] K. Mahmood, B. S. Swain, H. S. Jung, *Nanoscale* **2014**, *6*, 9127.
[20] a) H. Zhou, Q. Chen, G. Li, S. Luo, T.-b. Song, H.-S. Duan, Z. Hong, J. You, Y. Liu, Y. Yang, *Science* **2014**, *345*, 542; b) P. Qin, A. L. Domanski, A. K. Chandiran, R. Berger, H.-J. Butt, M. I. Dar, T. Moehl, N. Tetreault, P. Gao, S. Ahmad, M. K. Nazeeruddin, M. Grätzel, *Nanoscale* **2014**, *6*, 1508.
[21] M. Yang, R. Guo, K. Kadel, Y. Liu, K. O'Shea, R. Bone, X. Wang, J. He, W. Li, *J. Mater. Chem. A* **2014**, *2*, 19616.
[22] a) J. T.-W. Wang, J. M. Ball, E. M. Barea, A. Abate, J. A. Alexander-Webber, J. Huang, M. Saliba, I. Mora-Sero, J. Bisquert, H. J. Snaith, *Nano Lett.* **2013**, *14*, 724; b) Z. Zhu, J. Ma, Z. Wang, C. Mu, Z. Fan, L. Du, Y. Bai, L. Fan, H. Yan, D. L. Phillips, S. Yang, *J. Am. Chem. Soc.* **2014**, *136*, 3760.
[23] a) W. Ke, G. Fang, Q. Liu, L. Xiong, P. Qin, H. Tao, J. Wang, H. Lei, B. Li, J. Wan, G. Yang, Y. Yan, *J. Am. Chem. Soc.* **2015**, *137*, 6730; b) Y. Li, J. Zhu, Y. Huang, F. Liu, M. Lv, S. Chen, L. Hu, J. Tang, J. Yao, S. Dai, *RSC Adv.* **2015**, *5*, 28424; c) J. Song, E. Zheng, J. Bian, X.-F. Wang, W. Tian, Y. Sanehira, T. Miyasaka, *J. Mater. Chem. A* **2015**, *3*, 10837.
[24] C. G. Fonstad, R. H. Rediker, *J. Appl. Phys.* **1971**, *42*, 2911.
[25] D. Shi, V. Adinolfi, R. Comin, M. Yuan, E. Alarousu, A. Buin, Y. Chen, S. Hoogland, A. Rothenberger, K. Katsiev, Y. Losovyj, X. Zhang, P. A. Dowben, O. F. Mohammed, E. H. Sargent, O. M. Bakr, *Science* **2015**, *347*, 519.
[26] H. Yu, F. Wang, F. Xie, W. Li, J. Chen, N. Zhao, *Adv. Funct. Mater.* **2014**, *24*,7102.
[27] M. I. Dar, N. Arora, P. Gao, S. Ahmad, M. Grätzel, M. K. Nazeeruddin, *Nano Lett.* **2014**, *14*, 6991.
[28] Y. Tidhar, E. Edri, H. Weissman, D. Zohar, G. Hodes, D. Cahen, B. Rybtchinski, S. Kirmayer, *J. Am. Chem. Soc.* **2014**, *136*, 13249.
[29] S. T. Williams, F. Zuo, C.-C. Chueh, C.-Y. Liao, P.-W. Liang, A. K. Y. Jen, *ACS Nano* **2014**, *8*, 10640.
[30] a) H. J. Snaith, C. Ducati, *Nano Lett.* **2010**, *10*, 1259; b) Y. F. Wang, J. W. Li, Y. F. Hou, X. Y. Yu, C. Y. Su, D. B. Kuang, *Chem. Eur. J.* **2010**, *16*, 8620.
[31] a) E. L. Unger, E. T. Hoke, C. D. Bailie, W. H. Nguyen, A. R. Bowring, T. Heumuller, M. G. Christoforo, M. D. McGehee, *Energy Environ. Sci.* **2014**, *7*, 3690; b) H. J. Snaith, A. Abate, J. M. Ball, G. E. Eperon, T. Leijtens, N. K. Noel, S. D. Stranks, J. T.-W. Wang, K. Wojciechowski, W. Zhang, *J. Phys. Chem. Lett.* **2014**, *5*, 1511.
[32] a) J. H. Kim, P.-W. Liang, S. T. Williams, N. Cho, C.-C. Chueh, M. S. Glaz, D. S. Ginger, A. K. Y. Jen, *Adv. Mater.* **2014**, *27*, 695; b) Y. Chen, T. Chen, L. Dai, *Adv. Mater.* **2014**, *27*, 1053.
[33] S. H. Im, J.-H. Heo, H. J. Han, D. Kim, T. Ahn, *Energy Environ. Sci.* **2015**, *8*, 1602.
[34] J. M. Frost, K. T. Butler, F. Brivio, C. H. Hendon, M. Van Schilfgaarde, A. Walsh, *Nano Lett.* **2014**, *14*, 2584.
[35] S. Gubbala, V. Chakrapani, V. Kumar, M. K. Sunkara, *Adv. Funct. Mater.* **2008**, *18*, 2411.